Plant and Controller Optimization for Power and Energy Systems With Model Predictive Control

Donald J. Docimo[1]
Department of Mechanical Engineering,
Texas Tech University,
Lubbock, TX 79409
e-mail: donald.docimo@ttu.edu

Ziliang Kang
Department of Aerospace Engineering,
University of Illinois at Urbana-Champaign,
Urbana, IL 61801
e-mail: kang134@illinois.edu

Kai A. James
Department of Aerospace Engineering,
University of Illinois at Urbana-Champaign,
Urbana, IL 61801
e-mail: kaijames@illinois.edu

Andrew G. Alleyne
Department of Mechanical
Science and Engineering,
University of Illinois at Urbana-Champaign,
Urbana, IL 61801
e-mail: alleyne@illinois.edu

This article explores the optimization of plant characteristics and controller parameters for electrified mobility. Electrification of mobile transportation systems, such as automobiles and aircraft, presents the ability to improve key performance metrics such as efficiency and cost. However, the strong bidirectional coupling between electrical and thermal dynamics within new components creates integration challenges, increasing component degradation, and reducing performance. Diminishing these issues requires novel plant designs and control strategies. The electrified mobility literature provides prior studies on plant and controller optimization, known as control co-design (CCD). A void within these studies is the lack of model predictive control (MPC), recognized to manage multi-domain dynamics for electrified systems, within CCD frameworks. This article addresses this through three contributions. First, a thermo-electromechanical hybrid electric vehicle (HEV) powertrain model is developed that is suitable for both plant optimization and MPC. Second, simultaneous plant and controller optimization is performed for this multi-domain system. Third, MPC is integrated within a CCD framework using the candidate HEV powertrain model. Results indicate that optimizing both the plant and MPC parameters simultaneously can reduce physical component sizes by over 60% and key performance metric errors by over 50%. [DOI: 10.1115/1.4050399]

1 Introduction

This article addresses plant and controller optimization for power and energy systems. There is an ongoing shift in the expectations of mobile power systems such as vehicles and aircraft, which has promoted the development of partially or fully electrified vehicle architectures. In the U.S. transportation sector, electricity as an energy source is predicted to grow, on average, 7.4% per year up to 2050 [1]. Electrification of these systems is motived by its potential to meet new metrics: (a) Reduce greenhouse gas emissions [2] to meet future standards set by different countries [3]; (b) increase efficiency [4,5]; and (c) minimize fuel cost [5]. The electrification of mobility and transportation systems necessitates the introduction of new components into conventional designs. The dynamics of these new electrical components are strongly coupled to temperature [6–8], triggering integration issues that complicate overall performance and component degradation [9,10].

Offsetting these integration issues requires development of new (i) real-time control algorithms and (ii) plant design methodologies to maximize closed-loop plant performance for these dynamically complex systems. An additional possibility is the ability to develop both of these simultaneously, known as (iii) control co-design. As presented below, prior literature has explored several of these areas, usually in isolation from the overall system evaluation.

1.1 Advancements in Real-Time Control. The automotive literature presents several alternative strategies for energy management of powertrains with electromechanical dynamics. This includes iterative dynamic programming [11], stochastic dynamic programing [12,13], equivalent consumption minimization strategies [14,15], and rule-based strategies [16,17], as well as strategies enhanced by machine learning [18] and data-driven methods [19]. Some of these strategies have been extended to include consideration of component health [20], such as using stochastic dynamic programming to match desired outputs while minimizing energy cost and energy storage device degradation [21]. Building on this, recent studies include thermal dynamics of the cabin [22] and battery pack [23] under the supervision of the energy management controller. This allows for the consideration of the bidirectional coupling between electrical and thermal dynamics in hybrid electric vehicles (HEVs) and electric vehicles (EVs), mitigating integration issues. Real-time optimization algorithms are also explored to manage mechanical powertrain, engine coolant, and thermal cabin dynamics to reduce heating, ventilation, and air conditioning energy consumption [24]. Model-based algorithms such as model predictive control (MPC) are an alternative option to manage multi-domain dynamics of vehicles [25,26]. This includes hierarchical and distributed MPC architectures, which are particularly capable of managing timescale separation caused by fast electrical and slow thermal dynamics [27–30].

1.2 Advancements in Plant Design. Plant design can be categorized by studies focusing on sizing optimization and topology optimization. Sizing optimization seeks to optimize component sizes within the system, including thermal component design [31] and electromechanical components [32,33] within a vehicle. Topology generation and optimization seeks to adjust the configuration or architecture of the system components [34,35]. These methods can be combined to simultaneously optimize both the sizing and topology of the plant to maximize performance. The aircraft design literature also explores sizing and topology optimization, often with an emphasis on structural design [36–38].

1.3 Advancements in Control Co-Design. The optimization of plant and controller features, also referred to as control co-

[1]Corresponding author.

Contributed by the Dynamic Systems Division of ASME for publication in the Journal of Dynamic Systems, Measurement, and Control. Manuscript received October 14, 2020; final manuscript received January 12, 2021; published online April 7, 2021. Assoc. Editor: Mahdi Shahbahkti.

design (CCD), seeks to maximize closed-loop plant performance. Sequential optimization is used in practice often, where the plant design is first optimized, and then the controller design is then optimized for that plant [39]. This can be extended to an alternating or iterative procedure [40]. However, unless the plant design and controller design problems are separable, the optimal plant and controller variable values must be identified using simultaneous or nested optimization strategies [41]. CCD methods have been applied to automotive systems, with a focus on HEV powertrains with electromechanical dynamics. Studies include optimization of component sizes alongside the supervisory controller parameters [42,43], and optimization of the gear ratios and topology with a nested control problem [44].

The maturity of the electrified mobility literature provides studies on plant, controller, and CCD optimization strategies. However, there are three notable gaps in this literature. First, while there is a shift toward inclusion of thermal dynamics in the model, most studies emphasize electromechanical dynamics of these systems. Limiting the modeling of thermal dynamics in these systems does not address the integration issue of electrical components whose performance is highly dependent on temperature. Second, and as a result of the first gap, the application of CCD optimization frameworks has not been explored in detail for electrified mobility systems with thermal, electrical, and mechanical dynamics. Third, CCD frameworks center on nested control problems [44], and occasionally tune controller parameters as well [45]. However, studies of CCD with MPC have yet to be explored in detail for electrified mobility, being limited to chemical plant applications [46–48]. To apply CCD frameworks to electrified systems, the controller strategies embedded within CCD frameworks should be inclusive to the MPC strategies used within these systems.

This article addresses these gaps through three contributions to the literature:

(1) A thermo-electromechanical model of a power-split HEV powertrain is developed. This model captures the dynamics of the electrical and mechanical powertrain components, as well as the thermal management subsystem. The graph-based structure of the model lends itself to be easily implemented in design optimization frameworks, as well as development of MPC algorithms.
(2) Simultaneous plant and controller optimization is applied to systems with thermal, electrical, and mechanical dynamic elements, using the HEV powertrain model as the candidate system. The simultaneous optimization of the plant and controller design variables is compared against plant feature optimization and sequential optimization.
(3) MPC is embedded into the plant and controller optimization framework, reflecting the advanced control strategies appropriate for systems with multi-domain dynamics. This allows for the optimization of MPC parameters such as the time-step, preview, control input limits, and state tracking gains. This article will focus on centralized MPC, leaving extensions to hierarchical MPC and limited computational resources for future studies.

To develop these contributions, Sec. 2 reviews the graph-based modeling techniques used to create the HEV powertrain model. It also reviews a recently developed design optimization framework for connecting graph-based models to plant and controller design optimization. Sections 3 and 4 present the formulation of the MPC problem, and the CCD framework overview, respectively. Section 5 provides an overview of the thermo-electromechanical HEV powertrain model. In Sec. 6, the design optimization problem is formulated and the model under MPC control is validated for a base design. Section 7 presents the optimization results from (i) optimization of only the HEV powertrain plant design, (ii) sequential optimization of the plant and controller, and (iii) simultaneous optimization of the plant and controller. The article ends with a summary of the contributions and insights from the optimization studies.

2 Graph-Based Modeling and Design

This section reviews the techniques utilized to model multi-domain dynamic systems and perform optimization. Component and system dynamics are modeled using a conservation-based, graphical modeling technique. Optimization is performed using a four step design optimization framework based on modifying the elements in the graph-based models using design variables.

2.1 Graph-Based Modeling. The components and systems in this article are modeled using a modular graph-based modeling approach, with full descriptions presented in Refs. [49–52]. Figure 1 presents the elements of a graph-based model. A vertex represents an energy storage element, and is described by a storage capacitance C_i and a state x_i. An external vertex describes a state x_k^s with dynamics external to the model. An edge represents a power flow y_j, and is described by the nonlinear function f_j:

$$y_j = f_j\left(x_j^{\text{head}}, x_j^{\text{tail}}, u_j\right) \tag{1}$$

In Eq. (1), x_j^{head} is the state of the vertex at the head of the edge, x_j^{tail} is the state of the vertex at the tail of the edge, and u_j is an input. Note that all edges are not required to have an input. A graph with $i = 1, \ldots, N_v$ vertices, $j = 1, \ldots, N_e$ edges, and $k = 1, \ldots, N_t$ sink vertices is described by:

$$\boldsymbol{C}\dot{\boldsymbol{x}} = -\overline{\boldsymbol{M}}\boldsymbol{y} + \boldsymbol{D}\boldsymbol{y}^{\boldsymbol{s}} \tag{2}$$

In Eq. (2), $\boldsymbol{C} \in \mathbb{R}^{N_v \times N_v}$ is the diagonal matrix of storage capacitances, $\boldsymbol{x} \in \mathbb{R}^{N_v}$ is the vector of states, $\boldsymbol{y} \in \mathbb{R}^{N_e}$ is the vector of power flows, and $\overline{\boldsymbol{M}} \in \mathbb{R}^{N_v \times N_e}$ maps the power flows to the state vector. An entry of $\overline{\boldsymbol{M}}$ is $+1$ if a vertex is the tail of an edge, -1 if a vertex is a head of an edge, and 0 otherwise. Note that the models presented in this article do not feature source edge elements in the graph, and so $\boldsymbol{D} = 0$ and $\boldsymbol{y}^{\boldsymbol{s}} = 0$. These terms will be excluded for the remainder of this article.

The models presented in this article contain three types of vertices, described in Table 1. Type 1 vertices often describe thermal capacitances. Type 2 vertices typically describe inductances, electrical capacitances, inertias, and mechanical spring elements. Type 3 vertices are reserved for storage capacitances relating to

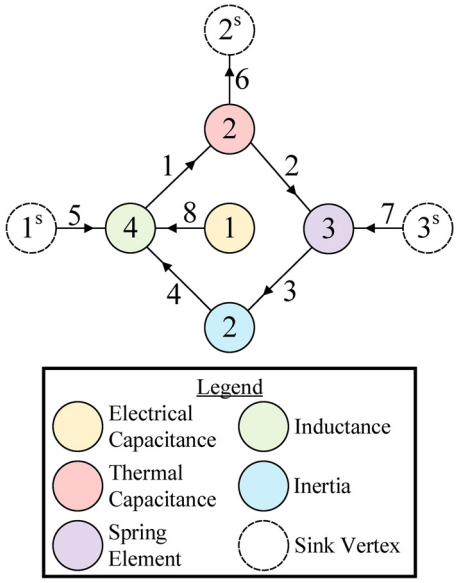

Fig. 1 Graph-based model with the primary elements

Table 1 Vertex types

Vertex type	Storage capacitance C_i
1	c_i
2	$c_i x_i$
3	$c_i(x_i)$

Table 2 Edge types

Edge type	Power flow y_j
1	$\alpha_j x_j^{\text{tail}}$
2	$\alpha_j x_j^{\text{head}}$
3	$\alpha_j x_j^{\text{tail}} x_j^{\text{head}}$
4	$\alpha_j \left(x_j^{\text{tail}}\right)^2$
5	$\alpha_j \left(x_j^{\text{tail}} - x_j^{\text{head}}\right)$
6	$\alpha_j \left(x_j^{\text{tail}}\right)^3$
7	$\alpha_j u_j x_j^{\text{tail}}$
8	$\alpha_j u_j x_j^{\text{tail}} x_j^{\text{head}}$

nonlinear behaviors, such as those found in batteries. Similarly, Table 2 presents the eight categories of edges used in the models of this work. Note that any of these edges can have a nonlinear expression for the parameter α_j.

2.2 Multi-Domain Design Optimization Framework. Plant and controller optimization is performed using a design optimization framework for multi-domain conservation-based systems [53]. Starting with a graph-based model described by Eq. (2), optimization is performed using four steps:

(1) The graph-based model is augmented with design matrices to describe sizing and topology changes, yielding Eq. (3). Sizing of elements is controlled by continuous plant design variables $\boldsymbol{\theta_c} \in \mathbb{R}^{N_c}$, and topology changes are controlled by discrete plant design variables $\boldsymbol{z} \in \mathbb{R}^{N_z}$. The design matrix $\boldsymbol{\Psi_c} \in \mathbb{R}^{N_v \times N_v}$ is a diagonal matrix that maps the continuous plant design variables to modifications of the storage capacitances. The matrix $\boldsymbol{\Phi_c} \in \mathbb{R}^{N_v \times N_v}$ acts similarly, but maps the discrete design variables to modifications of the storage capacitances. The matrix $\boldsymbol{\Psi} \in \mathbb{R}^{N_e \times N_e}$ is a diagonal matrix that maps the continuous variables to modifications of the power flows, and $\boldsymbol{\Phi} \in \mathbb{R}^{N_e \times N_e}$ is a diagonal matrix that maps the discrete variables to power flow modifications.

$$\boldsymbol{\Psi_c \Phi_c C \dot{x}} = -\overline{\boldsymbol{M}} \boldsymbol{\Psi \Phi y} \tag{3}$$

(2) The objective function is defined for optimization. Equation (4) defines the aggregate objective function J_{tot} for this work, with four individual objectives:

$$J_{\text{tot}} = w_{\text{st}} J_{\text{st}}^m + w_{\text{sc}} J_{\text{sc}}^m + w_{\text{en}} J_{\text{en}}^m + w_{\text{size}} J_{\text{size}}^m \tag{4}$$

Equation (5) defines the state tracking error objective, J_{st}, with weight w_{st}. The objective is evaluated at discrete times $j = 1, \ldots, N_{\text{final}}$ with time-step Δt_e and final time $t_{\text{final}} = N_{\text{final}} \Delta t_e$. The vector $\boldsymbol{r} \in \mathbb{R}^{N_v}$ contains the reference states, and the matrix $\boldsymbol{\Lambda_x} \in \mathbb{R}^{N_v \times N_v}$ internally weighs the individual reference state errors, with $\|\boldsymbol{x}\|_{\boldsymbol{\Lambda_x}}^2 = \boldsymbol{x}^T \boldsymbol{\Lambda_x} \boldsymbol{x}$. The function is normalized by a selected constant $\overline{J}_{st}$, which will allow expected J_{st} values to be in the range of 0–20 in this work. Similar normalization terms will be used for the remaining individual objectives to yield values of similar magnitude.

$$J_{\text{st}} = \frac{1}{\overline{J}_{\text{st}}} \sum_{j=1}^{N_{\text{final}}} \|\boldsymbol{x}_j - \boldsymbol{r}_j\|_{\boldsymbol{\Lambda_x}}^2 \tag{5}$$

Equation (6) defines the state constraint violations objective, J_{sc}, with weight w_{sc}, evaluated at the same times as J_{st}. The slack variables $\boldsymbol{s} \in \mathbb{R}^{N_v}$ are equal to the maximum of $\left[\left|x_i - x_{\min,i}\right|, \left|x_i - x_{\max,i}\right|\right]$ for state x_i, with $x_{\min,i}$ and $x_{\max,i}$ as the minimum and maximum allowable state values, respectively. The matrix $\boldsymbol{\Lambda_s} \in \mathbb{R}^{N_v \times N_v}$ internally weighs the terms. The function is normalized by a selected constant $\overline{J}_{\text{sc}}$.

$$J_{\text{sc}} = \frac{1}{\overline{J}_{\text{sc}}} \sum_{j=1}^{N_{\text{final}}} \|\boldsymbol{s}_j\|_{\boldsymbol{\Lambda_s}}^2 \tag{6}$$

Equation (7) defines the energy utilization objective, J_{en}, with weight w_{en}. This function relates to the total energy passing through the edges over the test period, with the integral evaluated using the trapezoidal rule with the same time interval as J_{st}. The matrix $\boldsymbol{\Lambda_p} \in \mathbb{R}^{N_e \times N_e}$ internally weighs the terms, with $\Lambda_{p,j,j}$ as the internal weight for edge j. The function is normalized by a selected constant $\overline{J}_{\text{en}}$.

$$J_{\text{en}} = \frac{1}{\overline{J}_{\text{en}}} \sum_{j=1}^{N_e} \left(\int_0^{t_{\text{final}}} \Lambda_{p,j,j} y_j(t) dt \right) \tag{7}$$

These first three objectives are calculated by evaluating the dynamics of the system under open-loop or closed-loop control. Equation (8) describes the final objective J_{size}, with weight w_{size}, to minimize the size of the continuous plant design variables, with internal weights $\boldsymbol{w_c}$. The function is normalized by a selected constant $\overline{J}_{\text{size}}$.

$$J_{\text{size}} = \frac{1}{\overline{J}_{\text{size}}} \boldsymbol{w_c \theta_c} \tag{8}$$

These four objectives are chosen to directly capture important performance, efficiency, and sustainability metrics for automotive applications. For identification of optimal designs for nonconvex problems, the integer $m = 4$ is used for compromise programming [54] when optimizing, as Eq. (4) shows.

(3) The constraints for the optimization problem are defined. The plant design variables $\boldsymbol{\theta_c}$ and $\boldsymbol{z}$ are bounded between minimum values $\underline{\boldsymbol{\theta_c}}$ and $\underline{\boldsymbol{z}}$, and maximum values $\overline{\boldsymbol{\theta_c}}$ and $\overline{\boldsymbol{z}}$. In addition, to optimize controller parameters, the controller design variables $\boldsymbol{\phi} \in \mathbb{R}^{N_\phi}$ are defined [55]. These have minimum and maximum bounds $\underline{\boldsymbol{\phi}}$ and $\overline{\boldsymbol{\phi}}$, respectively. Equation (9) defines the constraints.

$$\begin{aligned} \underline{\boldsymbol{\theta_c}} \le \boldsymbol{\theta_c} \le \overline{\boldsymbol{\theta_c}} \\ \underline{\boldsymbol{z}} \le \boldsymbol{z} \le \overline{\boldsymbol{z}} \\ \underline{\boldsymbol{\phi}} \le \boldsymbol{\phi} \le \overline{\boldsymbol{\phi}} \end{aligned} \tag{9}$$

(4) The optimization problem is formulated using the previous three steps and solved. The shooting method is used by simulating the dynamics of Eq. (3) and evaluating the objective function of Eq. (4). Design variables are updated to ensure the constraints of Eq. (9) are met.

3 Model Predictive Control Formulation

This section reviews the formulation of the centralized MPC problem [28,56]. This formulation is used to control the HEV

powertrain energy dynamics within the design optimization process. In this work, the powertrain dynamics are applied assuming an autonomous system. This will permit the controller to make tradeoffs between state tracking and state constraint violations during operation. The prediction model for MPC is determined by linearizing the augmented graph-based model of Eq. (3) about a given time index p. Linearization is performed about the most recent operating states and inputs of the system at time index k, i.e., $p = k$. As some storage capacitances are potentially zero, this creates a set of differential algebraic equations (DAEs), which are discretized temporarily using the forward Euler method and time-step Δt. Equation (10) presents the linearized, discretized model equations, with $\boldsymbol{\mathcal{C}}_p \in \mathbb{R}^{N_v \times N_v}$ as a diagonal matrix akin to the capacitance matrix. The matrices $\boldsymbol{A}_p \in \mathbb{R}^{N_v \times N_v}$ and $\boldsymbol{B}_p \in \mathbb{R}^{N_v \times N_u}$ are similar to the state and input matrices, respectively, of state space models. The column vector $\boldsymbol{u} \in \mathbb{R}^{N_u}$ contains N_u inputs. The matrix $\boldsymbol{V}_p \in \mathbb{R}^{N_v \times N_t}$ describes how external states impact the dynamics, $\boldsymbol{x}^s \in \mathbb{R}^{N_t}$ are the external states, and $\boldsymbol{W}_p \in \mathbb{R}^{N_v}$ describes constant terms created from linearization about a nonequilibrium point.

$$\boldsymbol{\mathcal{C}}_p \boldsymbol{x}_{k+1} = (\boldsymbol{\mathcal{C}}_p + \Delta t \boldsymbol{A}_p)\boldsymbol{x}_k + \Delta t \boldsymbol{B}_p \boldsymbol{u}_k + \Delta t \boldsymbol{V}_p \boldsymbol{x}_k^s + \Delta t \boldsymbol{W}_p \tag{10}$$

To stabilize the discrete model for a given time-step, model reduction can be performed. This work residualizes faster states by setting entries of $\boldsymbol{\mathcal{C}}_p$ below a minimum value to 0.

Equation (11) defines the optimization problem solved for each time the controller is called, over a prediction horizon of N_p steps. The decision variables are the inputs $\overline{\boldsymbol{u}}_k = [\boldsymbol{u}_{k|k}, \ldots, \boldsymbol{u}_{k+N_p-1|k}]$, the states $\overline{\boldsymbol{x}}_k = [\boldsymbol{x}_{k|k}, \ldots, \boldsymbol{x}_{k+N_p|k}]$, and the slack variables $\overline{\boldsymbol{s}}_k = [\boldsymbol{s}_{k|k}, \ldots, \boldsymbol{s}_{k+N_p-1|k}]$. The first constraint of Eq. (11) defines the state dynamics. The second through fourth constraints describe the conditions of the slack variables for the soft constraints. The fifth constraint bounds the inputs between $\boldsymbol{u}_{\min}$ and $\boldsymbol{u}_{\max}$. The sixth constraint is to keep inputs within a range of the previous set of inputs sent to the system, $\boldsymbol{u}_{\text{prev}}$, using variable $0 \le \varepsilon \le 1$. This acts similar to a rate limit, but as a tighter input bound over the prediction horizon. The seventh constraint fixes certain inputs to be equal to state values, using matrices $\boldsymbol{Z}_1 \in \mathbb{R}^{N_u \times N_u}$ and $\boldsymbol{Z}_2 \in \mathbb{R}^{N_u \times N_v}$. This is used to relate pump and fan speeds to mass flow rates. The eighth constraint provides the final value for the algebraic states $\boldsymbol{x}^a$ at index $k + N_p$, which cannot be calculated without knowledge of inputs at this time index. The final constraint sets the initial conditions for the dynamic states $\boldsymbol{x}^d$, provided from the plant dynamics when the controller is called.

$$\begin{aligned}
J_k^* = \min_{\overline{\boldsymbol{u}}_k, \overline{\boldsymbol{x}}_k, \overline{\boldsymbol{s}}_k} \quad & J_k \\
\text{subject to } \forall j \in [0, N_p - 1] \quad & \boldsymbol{\mathcal{C}}_k \boldsymbol{x}_{k+j+1|k} = (\boldsymbol{\mathcal{C}}_k + \Delta t \boldsymbol{A}_k)\boldsymbol{x}_{k+j|k} + \Delta t \boldsymbol{B}_k \boldsymbol{u}_{k+j|k} + \Delta t \boldsymbol{V}_k \boldsymbol{x}^s_{k+j|k} + \Delta t \boldsymbol{W}_k \\
& \boldsymbol{x}_{\min} - \boldsymbol{s}_{k+j|k} \le \boldsymbol{x}_{k+j+1|k} \\
& \boldsymbol{x}_{k+j+1|k} \le \boldsymbol{x}_{\max} + \boldsymbol{s}_{k+j|k} \\
& \boldsymbol{s}_{k+j|k} \ge 0 \\
& \boldsymbol{u}_{\min} \le \boldsymbol{u}_{k+j|k} \le \boldsymbol{u}_{\max} \\
& (1-\varepsilon)\boldsymbol{u}_{\text{prev}} \le \boldsymbol{u}_{k+j|k} \le (1+\varepsilon)\boldsymbol{u}_{\text{prev}} \\
& \boldsymbol{Z}_1 \boldsymbol{u}_{k+j|k} = \boldsymbol{Z}_2 \boldsymbol{x}_{k+j|k} \\
& \boldsymbol{x}^a_{k+N_p|k} = \boldsymbol{x}^a_{k+N_p-1|k} \\
& \boldsymbol{x}^d_{k|k} = \boldsymbol{x}^d_k
\end{aligned} \tag{11}$$

Equation (12) defines the objective function J_k at time index k, which is an aggregate of two terms. The first term represents state tracking error with weighting matrix $\boldsymbol{\Lambda}_{x,c}$, while the second represents state constraints with weighting matrix $\boldsymbol{\Lambda}_{s,c}$. These functions are similar to Eqs. (5) and (6), but are evaluated only over the horizon of N_p steps. The predicted state vector for calling the controller at time index k is $\boldsymbol{x}_{k+j|k}$, for $j = 0, \ldots, N_p$.

$$J_k = \sum_{j=0}^{N_p} \|\boldsymbol{x}_{k+j|k} - \boldsymbol{r}_{k+j|k}\|^2_{\boldsymbol{\Lambda}_{x,c}} + \sum_{j=0}^{N_p-1} \|\boldsymbol{s}_{k+j|k}\|^2_{\boldsymbol{\Lambda}_{s,c}} \tag{12}$$

4 Control Co-Design Framework

This section explains the optimization procedure used for control co-design in this article. This work uses a genetic algorithm (GA) to optimize the values of the plant and controller design variables. However, the core concept is applicable to other optimization techniques, such as gradient-based searches. Figure 2 presents the procedure to optimize the design variable values. To begin, the engineer identifies which of the design variable values should be optimized, and which should be fixed at constant values. This permits optimization of only plant design variable values or only controller design variable values if desired. The initial population of designs is generated by augmenting the graph-based model and replacing the controller design variable values. The objective function is determined using the shooting method, i.e., simulating the dynamics for each design separately and calculating the objective function. When simulating a design, the MPC algorithm is run within an inner, nested loop to determine control inputs and plant dynamics. Once the simulation is complete, J_{tot} is evaluated. The stoppage criteria are checked, and if not met, the GA's selection, crossover and mutation functions are run to generate a new population. This continues the outer loop optimization process until the stoppage criteria are met, after which the optimized design variable values are output.

Figures 3 and 4 present the optimization techniques used in this article for the studies. Plant design optimization fixes the controller design variable values, and optimizes only the plant design variable values. Controller design optimization fixes the plant design variable values, and optimizes only the controller design variable values. Sequential CCD optimization is plant design optimization followed by controller design optimization. Simultaneous CCD optimization does not fix any design variable values. The plant and controller design variable values are optimized simultaneously to identify new designs.

5 Hybrid Electric Vehicle Powertrain Model

This section presents a thermo-electromechanical model of a candidate HEV powertrain with cooling. Note that the optimization procedures of this article are not specific to this configuration, and other powertrain layouts could be substituted for different studies. To retain clarity for this article, the full description of the model is provided in Supplemental Material on the ASME Digital Collection for this article. The HEV powertrain model is built by combining graph-based models of individual components. The components are separated into four categories. The first category contains components that operate primarily with electrical dynamics. This includes batteries, buses, and power electronics such as inverters, rectifiers, and DC–DC converters. The second category contains components that operate primarily with mechanical dynamics, including the motors and generators, pumps and fans, planetary gears and transmissions, and engines. The third category contains components with thermal dynamics, such as vapor compression systems (VCS) and cooling loops. The fourth category contains connector graphs that enable the combination of separate component graphs, such as gearboxes, radiators, and virtual inductors to maintain proper graph-based modeling format [51]. Multiple versions of component graphs are used within the model (e.g., there are multiple DC/DC converters).

Figures 5 and 6 present the configuration of the full thermo-electromechanical model of the power-split HEV powertrain with

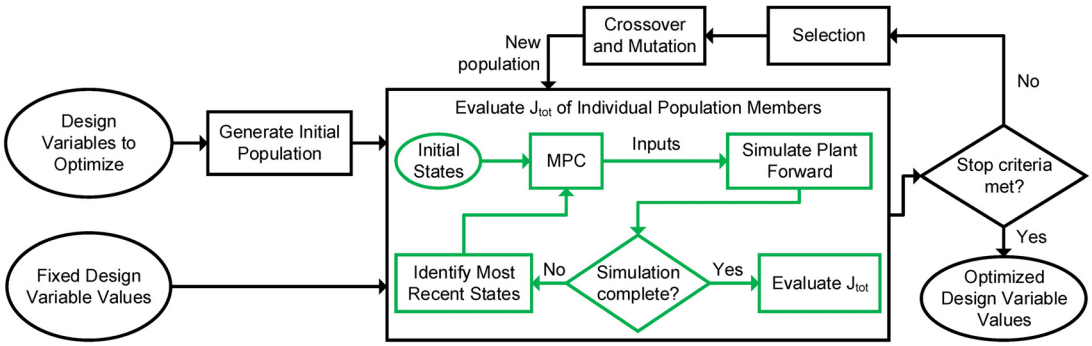

Fig. 2 Flowchart of the design optimization procedure using a genetic algorithm, with a black outline for the GA and a light green outline for the simulation of the model and embedded MPC

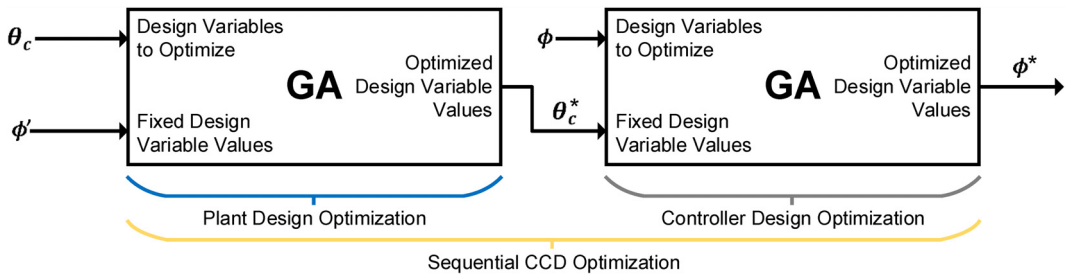

Fig. 3 Plant design, controller design, and sequential CCD optimization. The superscripts * and ' indicate an optimally identified set of values, and a nominal set of values, respectively.

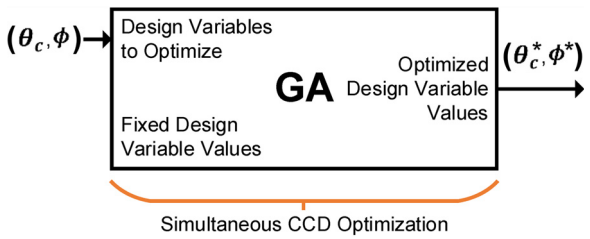

Fig. 4 Simultaneous CCD optimization. The superscript * indicates an optimally identified set of values.

cooling. Component models are interconnected to produce the full model, using a graphical composition method [57]. Graph interconnections are defined primarily using edge equivalencies: two edges, each from different graphs, are defined to be combined. The head and tail vertices of the edge from the first graph are matched to the tail and head vertices, respectively, of the second graph, defining vertex equivalencies. As the two combined edges can have different parameters or be of different types, one graph's edge is defined to be the dominant one used in the combined model. The Supplemental Material on the ASME Digital Collection lists all component graphs used and defines the edge equivalencies and dominant edges to create the full HEV powertrain model.

As shown in Figs. 5 and 6, the two main energy sources of the powertrain are the battery pack and the engine. The battery pack is connected to the high voltage bus in parallel. The high voltage bus connects to an inverter to power and control the motor, as well as a rectifier, which connects to the generator. The generator and engine are coupled through the planetary gear, and the planetary gear connects to the motor through the transmission. The transmission ultimately powers the wheels and propels the vehicle chassis, which are modeled together. The high voltage bus also connects to a DC/DC converter to power the low voltage bus. The low voltage bus is connected to six additional DC/DC converters, which power the pumps, fans, and compressor for the VCS. The battery, motor, generator, and each power electronics device have their own defined temperature state. In addition, the planetary gear has a temperature state to represent the thermal capacitance of the gear and the surrounding elements.

The cooling system contains four loops. The power electronics, which can have heat interactions between each other, is cooled by the power electronics cooling loop. The transaxle cooling loop rejects heat from the motor, generator, and planetary gear through parallel channels. The vapor compression system cooling loop cools the air passing through to the cabin, as well as the battery cooling loop liquid. The battery is cooled by its cooling loop. Air entering moves through a path within the vehicle, picking up heat as it passes by each heat exchanger. The loops and air within the paths are separated into multiple control volumes, meaning there are temperature states for different sections of the coolant.

6 Problem Setup

This section defines the design optimization problem for the HEV powertrain with cooling. Six plant design variables and three controller design variables are selected. Using baseline design variable values, the plant dynamics operating under the MPC algorithm are validated.

6.1 Problem Formulation. Six plant design variables are defined to optimize for the HEV powertrain system:

(1) $\theta_{c,1}$ is size of the heat exchanger near the battery.
(2) $\theta_{c,2}$ is size of the heat exchanger near the power electronics box.
(3) $\theta_{c,3}$ is size of the heat exchanger near the motor.
(4) $\theta_{c,4}$ is size of the heat exchanger near the generator.
(5) $\theta_{c,5}$ is size of the heat exchanger near the planetary gear box.
(6) $\theta_{c,6}$ is the size of the battery pack. To capture this, it describes the number of battery cells in parallel within the battery pack. This also scales the mass of the vehicle to account for larger battery pack sizes.

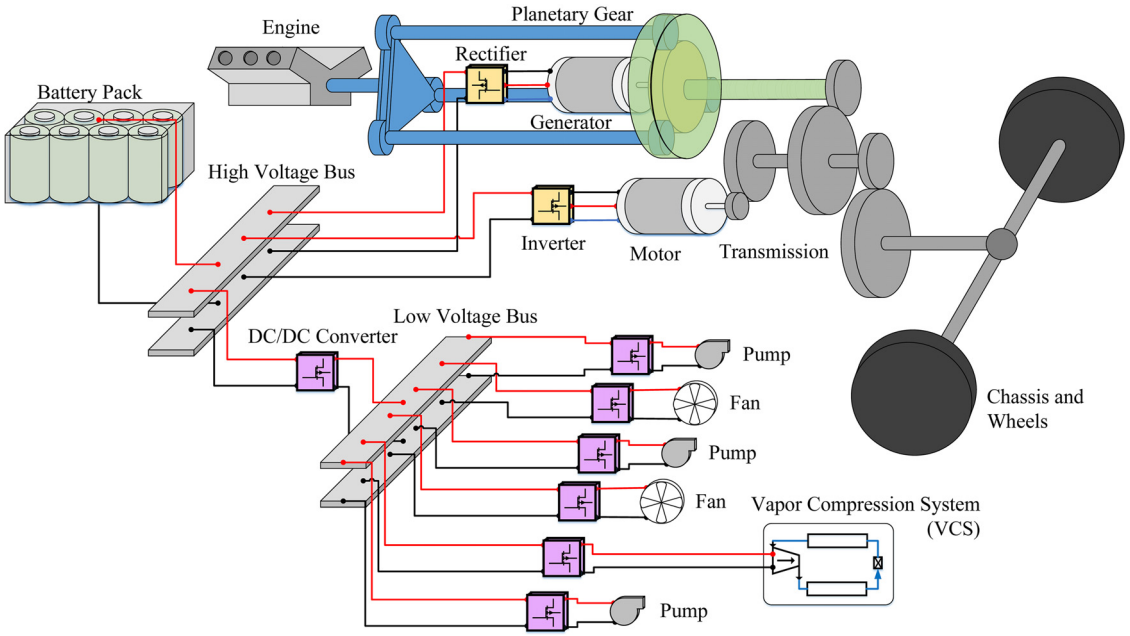

Fig. 5 Electromechanical configuration of the HEV powertrain

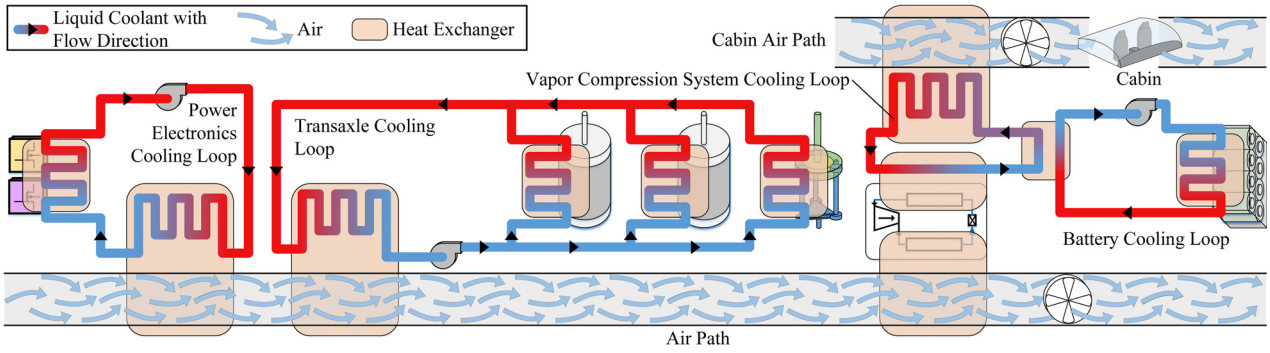

Fig. 6 Thermal cooling system for the HEV

A detailed description of how these relate to $\mathbf{\Psi_c}$ and $\mathbf{\Psi}$ is provided in Supplemental Material on the ASME Digital Collection. While the design framework is inclusive of topology optimization, such as selection of air versus liquid cooling [53], it is not performed in this work. As such, there are no discrete plant design variables, and $\mathbf{\Phi_c}$ and $\mathbf{\Phi}$ are both equal to the identity matrix. Equations (13) and (14) present the constraints for the plant design variables.

$$\underline{\boldsymbol{\theta_c}} = [0.1,\ 0.1,\ 0.1,\ 0.1,\ 0.1,\ 1]^T \tag{13}$$

$$\overline{\boldsymbol{\theta_c}} = [100,\ 100,\ 100,\ 100,\ 100,\ 10]^T \tag{14}$$

Three controller design variables are defined, with discrete options for each:

(1) $\phi_1 = \Delta t$ is the time-step for the controller. It is constrained to values of 0.5, 1, 2, and 3.
(2) ϕ_2 is the allowable perturbation of inputs from the last input, e.g., $\phi_2 = \varepsilon$. This controller design variable is constrained to 0.2, 0.25, 0.3, 0.35, and 0.4.
(3) ϕ_3 is the internal weight within $\mathbf{\Lambda}_{x,c}$ relating to velocity tracking. It is constrained to the following values: 10, 25, 50, 100–1000 in increments of 100, 1500, 2000, 3000, 5000, 10,000, 50,000, and 100,000.

The values of the controller design variables were selected to provide a grid to effectively explore the design space without increasing computational requirements to intractable levels. The design objective functions are the same as those presented in Eqs. (4)–(8), with 0.5 used for w_{st}, w_{sc}, w_{en}, and w_{size}. The normalization terms are $\bar{J}_{st} = 10^7$, $\bar{J}_{sc} = 10^{10}$, $\bar{J}_{en} = 10^7$, and $\bar{J}_{size} = 10^1$. These values are selected from preliminary testing to normalize the objective function values. Adjusting the weights or the normalization terms will impact the final plant and controller designed, though the methods presented remain applicable for all cases, and previous studies explore the impact of weights on designs [53]. State tracking error focuses on tracking vehicle velocity with a weighting of 100. The battery surface temperature is constrained between 20 °C and 40 °C. The motor and generator temperatures are constrained between 0 °C and 80 °C, and the power electronics temperatures are constrained between 10 °C and 110 °C. All temperature constraints have an internal weight of 1.4×10^3. The battery state of charge (SOC) is constrained between 0.3 and 0.7, with an internal weight of 1.4×10^5. These internal weights are selected such that 1 °C and 1% SOC violations give equal contributions to the state constraint violations objective. Total energy utilization is determined from battery edges 4–6 and 8, and engine edge 1, yielding the total energy used while driving. For the sizing objective, $\boldsymbol{w_c}$ factors the heat exchanger sizes equally with internal values of 1, and an internal value of 0 for the battery pack size.

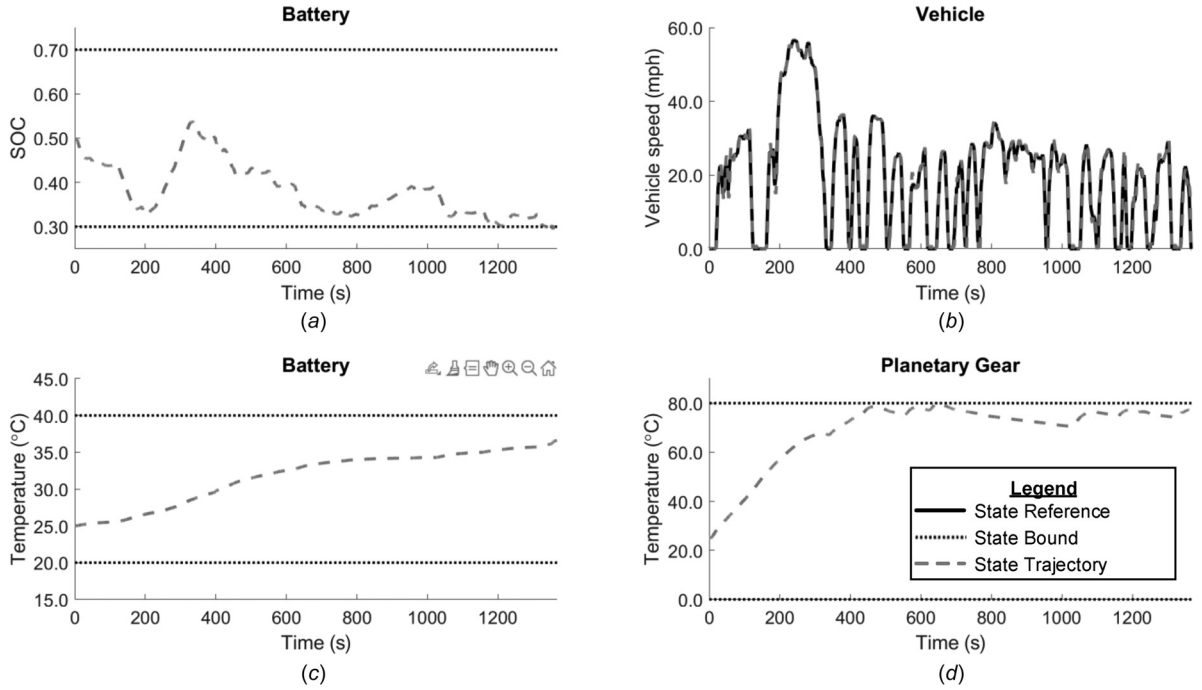

Fig. 7 (*a*) Battery SOC, (*b*) velocity, (*c*) battery surface temperature, and (*d*) planetary gear temperature for model and controller validation

The controller tracks the desired velocity with internal weight ϕ_3, and contains the same constraints and internal weights as the design optimization problem. The duty cycles for the power electronics make up a majority of the inputs for the system. The duty cycle for the converter between the high and low voltage buses is limited between 0.19 and 0.2, while the duty cycle input for the converter connected to the VCS is limited between 0.09 and 0.1. The duty cycle for converters powering fans and pumps are limited to 0.04–0.05 and 0–0.3, respectively. These input constraints permit the components powered by these converters to operate in their appropriate power ranges, drawn from preliminary analysis. The inverter duty cycle, rectifier duty cycle, engine throttle, and brake command are all limited between 0 and 1. The input to each cooling system and air path is the mass flow rate, which is dependent on the speed of the pump or fan connected to it. Model reduction is performed by setting entries of $\boldsymbol{C_p}$ less than 100 to be 0. This minimum value is chosen in part due to its ability to yield a stable model for all potential values of ϕ_1. The controller operates with a horizon $N_p = 4$ steps. In addition, the first two inputs provided from the controller are used before calling the controller again, with $\boldsymbol{u}_{\text{prev}} = \boldsymbol{u}_{k+1|k-1}$.

6.2 Model and Controller Validation. The model and centralized MPC algorithm are validated using a base set of plant and controller design variables. The Urban Dynamometer Driving Schedule (UDDS) drive cycle is used to define a desired vehicle velocity. Ambient temperature profiles are at a constant 25 °C, with all other external state profiles set to zero. In this example, $\theta_{c,1} = \ldots = \theta_{c,5} = 100$, $\theta_{c,6} = 3$, $\phi_1 = 1$, $\phi_2 = 0.25$, and $\phi_3 = 100$. The MATLAB `ode23tb` solver is used to solve the system, with analytical solutions provided for the algebraic state equations.

Figure 7 presents the state trajectories for the battery SOC, vehicle velocity, and battery temperature. The planetary gear temperature is also plotted as it has a low thermal capacitance, but high power passing through it during operation, making temperature control difficult. The plant configuration and controller are able to track the desired vehicle velocity, with an average error of 1.20 mph and standard deviation of 1.34 mph, with error defined as the absolute value of the difference of the reference and actual. State constraint violations are minimal, with maximum violations of 0.0084 for battery SOC, 0 °C for battery temperature, and 0.14 °C for the planetary gear. The motor, generator, and power electronics all remain within their temperature constraints.

7 Optimization Results

This section presents optimization results for the thermo-electromechanical HEV powertrain model with MPC. The plant and controller design variables are optimized for the UDDS drive cycle. Three studies are performed using a GA to optimize, with a population size of 10X the number of design variables being adjusted. The first study identifies the six plant design variable values for fixed controller design variable values. The second two studies perform two versions of CCD, including sequential optimization and simultaneous optimization of the plant and controller design variables. Results are presented to show the improvements in performance of the plant with controller.

Table 3 Design variables and objective function values for the initial and plant-optimized systems

	Initial design	Optimized plant design
$\theta_{c,1}$	22.5	38.2
$\theta_{c,2}$	7.91	1.56
$\theta_{c,3}$	73.2	0.639
$\theta_{c,4}$	29.7	8.64
$\theta_{c,5}$	16.9	13.7
$\theta_{c,6}$	7.28	4.35
ϕ_1	1	1
ϕ_2	0.25	0.25
ϕ_3	100	100
J_{st}	13.1	10.7
J_{sc}	0	0
J_{en}	1.48	1.25
J_{size}	15.0	6.28
J_{tot}	14.8	9.10

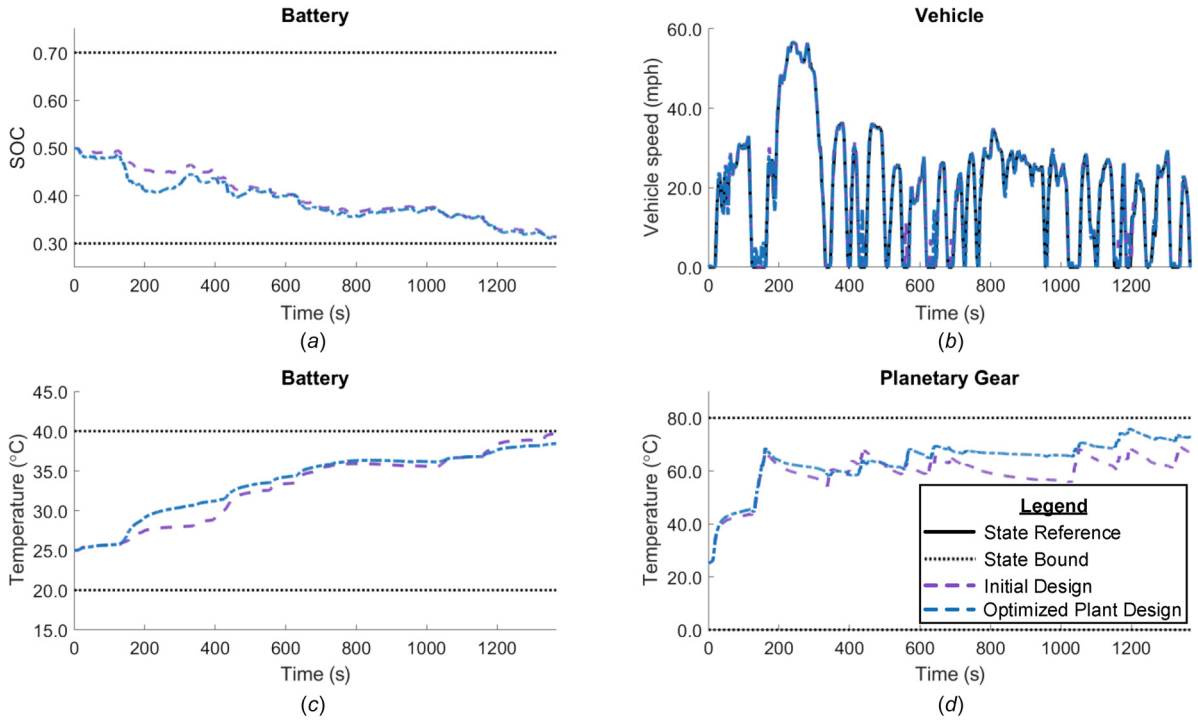

Fig. 8 (*a*) Battery SOC, (*b*) velocity, (*c*) battery surface temperature, and (*d*) planetary gear temperature for the best initial design and the optimized plant design

7.1 Plant Optimization With the UDDS Drive Cycle. Optimization using the UDDS drive cycle is first performed by optimizing the plant design variables with fixed controller design variables, using the values of $\phi_1 = 1$, $\phi_2 = 0.25$, and $\phi_3 = 100$. Optimization is performed using the MATLAB `ga` function with a population size of 60 and default settings. A computing cluster node with 192 GB of memory and 36 cores is used to run the optimization process in parallel. A total of 30 populations were generated, with 1800 function evaluations total. The total computing runtime for the optimization algorithm was 15 days. The set of design variables with the lowest total objective function value was generated in the 11th population.

Table 3 presents the design variables and objective function values for the designs with the lowest objective function values from the first population (initial design) and the final population (optimized plant design). Figure 8 presents the SOC, velocity, battery temperature, and planetary gear temperature state trajectories for both of these system designs. The average velocity tracking error is 1.41 mph for the initial design, with a standard deviation of 1.70 mph. The average error and standard deviation are 1.26 mph and 1.54 mph, respectively, for the optimized plant design. Neither design violates state constraints. There is a 58.2% reduction in the size of the heat exchangers after optimizing for the plant design variables. The total objective function is reduced by 38.6%. The initial and optimized plant designs have different pack sizes, with $\theta_{c,6}$ as 7.28 and 4.35, respectively, through similar SOC trends. This is due to the hybrid nature of the powertrain, with the engine providing more energy for powertrains with smaller packs.

7.2 Plant and Controller Optimization. To quantify the advantage conferred by control co-design, we compare the results of plant-only optimization against sequential and simultaneous optimization of the plant and controller design variables values. Sequential optimization uses a GA to identify the controller design variables values after identifying plant design variable values. The plant design variables are fixed, using the values identified from the optimized plant of Sec. 7.1. Simultaneous optimization describes the study which identifies the values for plant and controller design variables simultaneously using a GA.

Table 4 Design variables and objective function values for the sequential and simultaneous control co-design systems

	Sequential CCD-MPC design	Simultaneous CCD-MPC design
$\theta_{c,1}$	38.2	20.2
$\theta_{c,2}$	1.56	4.41
$\theta_{c,3}$	0.639	11.6
$\theta_{c,4}$	8.64	17.5
$\theta_{c,5}$	13.7	2.89
$\theta_{c,6}$	4.35	7.76
ϕ_1	1	0.5
ϕ_2	0.25	0.2
ϕ_3	1000	1000
J_{st}	7.69	5.58
J_{sc}	0	0.0752
J_{en}	1.24	1.32
J_{size}	6.28	5.66
J_{tot}	7.60	6.32

For the sequential optimization study, an additional ten populations of size 30 were evaluated after the optimization of the plant design variables, adding 300 to the earlier 1800 function evaluations. The total number of function evaluations was 2100, and the best controller design variables were generated in the third population. For the simultaneous optimization study, the GA was run for 20 generated populations of size 90, for a total of 1800 function evaluations.

Table 4 presents the design variables and objective function values using sequential and simultaneous optimization of the plant and controller design variables (sequential and simultaneous CCD-MPC, respectively). Both reduce the total objective function as compared to the system determined from solely optimizing the plant design variables. However, the total objective function from the simultaneous method is 20% lower as compared to the sequential method. This is primarily due to the reduction the simultaneously identified system provides in state tracking error and heat

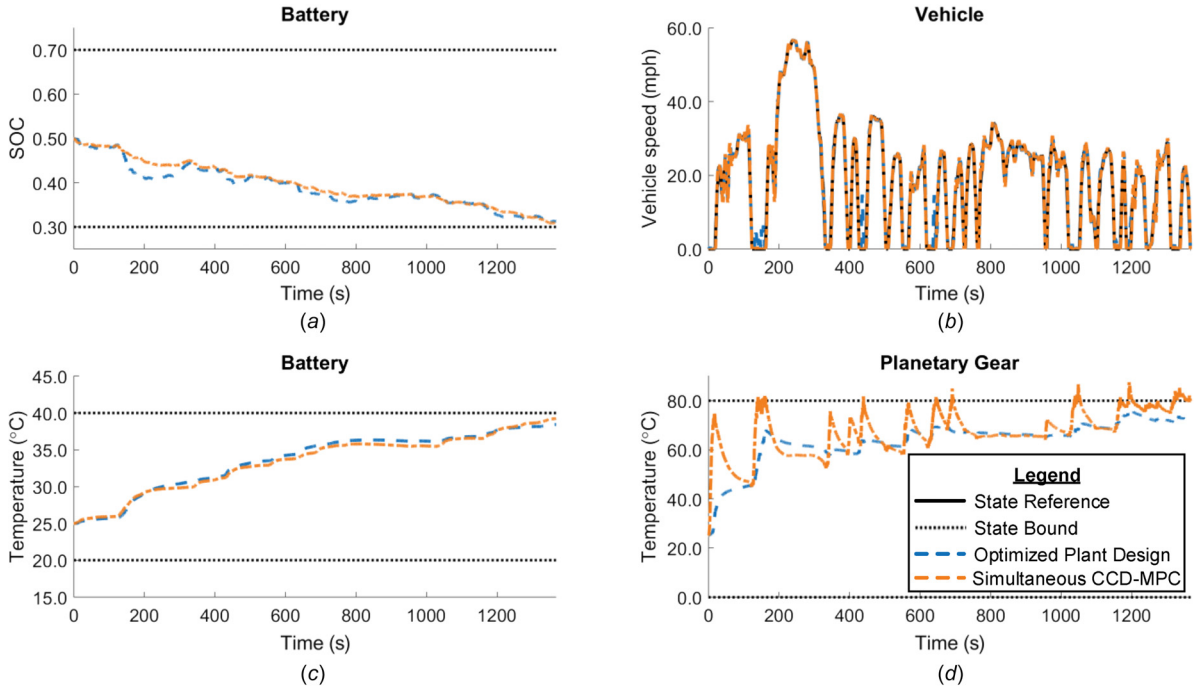

Fig. 9 (*a*) Battery SOC, (*b*) velocity, (*c*) battery surface temperature, and (*d*) planetary gear temperature for the optimized plant design and the design identified from simultaneous control co-design

exchanger sizes. Unlike sequential design, simultaneous CCD is able to optimally exploit the inherent design coupling between the plant and the controller. Figure 9 presents the state trajectories for the system identified using the simultaneous method as compared to the system identified from optimizing the plant only. As compared to the optimized plant design, the simultaneously identified design reduces state tracking error as Fig. 9(*b*) shows, with an average error of 0.99 mph and standard deviation of 1.05 mph. However, Fig. 9(*d*) indicates that the number of state constraint violations is increased in the planetary gear, reaching a maximum of 7.52 °C over the constraint for a brief period of time. This is a tradeoff that is determined by the relative weighting of the individual objective functions. The increase in state constraint violations is a relatively small increase in the total objective function, being 0.0376 after factoring in the weight w_{sc}. However, by doing so, the total size of the heat exchangers is reduced significantly, dropping the contribution of this to the total objective function by 0.31, an order of magnitude larger impact than the constraint violation.

Figure 10(*a*) presents a spider plot of the weighted individual objective functions (e.g., $w_{st}J_{st}, w_{sc}J_{sc}$) for each of the system designs. As shown, simultaneous optimization of the plant and controller design variables yields the largest reduction in the objective function, approaching closest to the unreachable utopia point. Sequential optimization of the plant and controller design variables does create improvements as compared to only

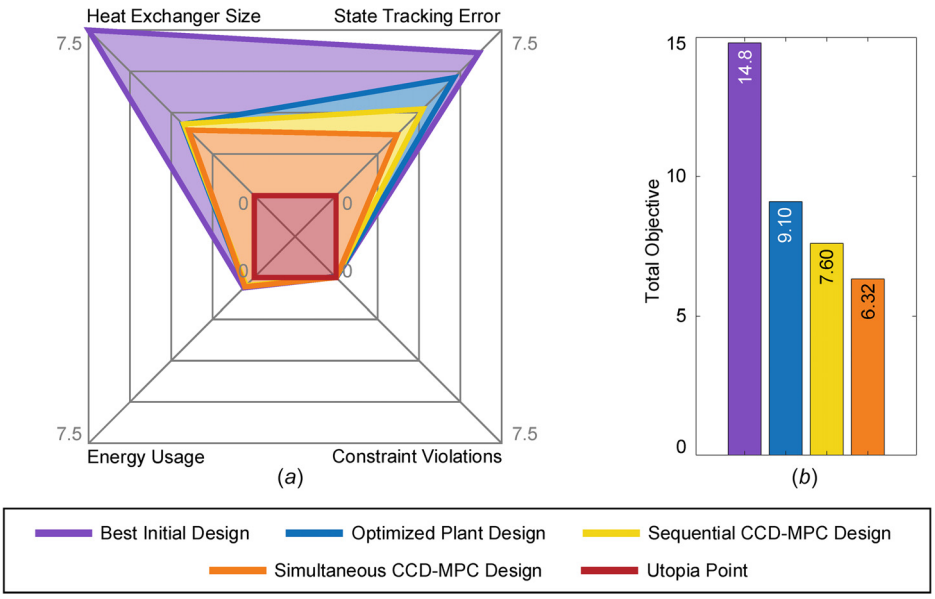

Fig. 10 Comparison of (*a*) the weighted individual objective function values and (*b*) the total objective function values for each design identified using different optimization strategies

Table 5 Reductions in objective function values as compared to the best initial design

	State tracking error (J_{st})	State constraint violations (J_{sc})	Energy used (J_{en})	Heat exchanger size (J_{size})	Total objective (J_{tot})
Optimized plant design	18.7% reduction	0.00% reduction	15.3% reduction	58.2% reduction	38.6% reduction
Sequential CCD-MPC	41.3% reduction	0.00% reduction	16.5% reduction	58.2% reduction	48.6% reduction
Simultaneous CCD-MPC	57.4% reduction	∞ increase	11.0% reduction	62.3% reduction	57.3% reduction

Darker shading indicates a relatively greater reduction as compared to the other designs.

optimization of the plant design, but not by as much as using simultaneous methods. The trend is reflected in Fig. 10(*b*), which plots the total objective function values ($m = 1$).

Table 5 quantifies how plant optimization, sequential plant and controller optimization, and simultaneous plant and controller optimization reduce the objective functions as compared to the best design from the initial population. Larger battery packs do seem to require more energy than smaller battery packs, though this is not validated in every case. This is because of the impact other design variables and control objectives have on the energy used. Simultaneous optimization reduces state tracking error by 57.4%, while sequential optimization and plant optimization reduce it by 41.3% and 18.7%, respectively. Simultaneous optimization reduces the total heat exchanger size by 62.3%, slightly more than the 58.2% from plant optimization. The tradeoffs made are that simultaneous optimization has a small, nonzero increase in state constraint violations (an infinite increase from 0), and a smaller reduction in energy used. However, these tradeoffs allow for a 57.3% reduction in the total objective function, as compared to a 38.6% reduction found by only performing plant optimization. This matches expectations: simultaneous optimization of plant and controller design variables yield superior designs as compared to only optimizing the plant, or optimizing the plant and the controller in a sequential fashion. These results indicate that this insight also applies to plants controlled by MPC algorithms.

8 Conclusions

This article explores CCD for power and energy systems with the integration of MPC. While the electrified mobility literature contains studies on plant and controller optimization for electromechanical powertrain dynamics, thermal dynamics are generally excluded. As electrical component performance is strongly coupled to temperature, this article expands on previous works by developing a novel thermo-electromechanical HEV powertrain model suitable for CCD. To utilize a controller recognized for handling thermal and electrical dynamics within these systems, a MPC algorithm is used to control the system dynamics.

Case studies optimize plant design variables, including heat exchanger and battery sizes, as well as controller design variables such as the MPC time-step, input limits, and MPC gains for tracking. Four individual objective functions, including heat exchanger size, state tracking error, constraint violations, and energy used, make up the total objective. Results show that optimization of the plant with a baseline MPC algorithm reduces heat exchanger size by 58.2% and state tracking error by 18.7% from an initial design. Optimization of both plant and controller design variables, either sequentially or simultaneously, further reduces the total objective. Simultaneous optimization provides the greatest reductions, with a 62.3% reduction in heat exchanger size and a 57.4% reduction in state tracking error, with a tradeoff of minimally more state constraint violations. The results indicate that embedding MPC into CCD frameworks can yield significant improvements in electrified vehicle performance. Future work will build on these results and integrate additional controller features, MPC parameters such as the prediction horizon, and plant dynamics into the design optimization process.

Acknowledgment

This material is based upon work supported by the National Science Foundation Engineering Research Center for Power Optimization of Electro-Thermal Systems (POETS) with cooperative agreement EEC-1449548. The authors thank Christopher T. Aksland for his valuable feedback during the development of the powertrain model.

Funding Data

- National Science Foundation Engineering Research Center for Power Optimization of Electro-Thermal Systems (POETS) (Agreement No. NSF EEC-14-49548).

Nomenclature

$\boldsymbol{A}$ = state matrix
$\boldsymbol{B}$ = input matrix
c = capacitance parameter
C = storage capacitance
$\boldsymbol{C}$ = storage capacitance matrix
$\boldsymbol{\mathcal{C}}$ = linearized capacitance matrix
$\boldsymbol{D}$ = source input matrix
f = nonlinear function
J = objective function
$\overline{J}$ = normalization parameter
m = compromise programing integer
$\overline{\boldsymbol{M}}$ = incidence matrix
N_c = number of continuous plant design variables
N_e = number of edges
N_p = prediction horizon
N_t = number of sink vertices
N_u = number of inputs
N_v = number of vertices
N_z = number of discrete plant design variables
N_ϕ = number of controller design variables
$\boldsymbol{r}$ = reference state vector
$\boldsymbol{s}$ = slack variables vector
$\overline{\boldsymbol{s}}$ = slack decision variables
u = input
$\boldsymbol{u}$ = input vector
$\overline{\boldsymbol{u}}$ = input decision variables
$\boldsymbol{u}_{\text{prev}}$ = previous input
$\boldsymbol{V}$ = matrix for how external states impact dynamics after linearization
w = weight
$\boldsymbol{W}$ = vector of constant terms from linearization
$\boldsymbol{w_c}$ = internal component weights
x = state
$\boldsymbol{x}$ = state vector
$\overline{\boldsymbol{x}}$ = state decision variables
$\boldsymbol{x^a}$ = algebraic states
$\boldsymbol{x^d}$ = dynamic states
x^{head} = head vertex state
x^s = external state
x^{tail} = tail vertex state
y = power flow
$\boldsymbol{y}$ = power flow vector

$\boldsymbol{y}^s$ = source power flow vector
$\boldsymbol{z}$ = discrete plant design variables
$\overline{\boldsymbol{z}}$ = upper bound on discrete plant design variables
$\underline{\boldsymbol{z}}$ = lower bound on discrete plant design variables
α = edge parameter
Δt = controller time-step
ε = allowable perturbation of inputs
$\boldsymbol{\theta_c}$ = continuous plant design variables
$\boldsymbol{\theta_c^*}$ = optimally identified continuous plant design variable values
$\overline{\boldsymbol{\theta_c}}$ = upper bound on continuous plant design variables
$\underline{\boldsymbol{\theta_c}}$ = lower bound on continuous plant design variables
$\boldsymbol{\Lambda_p}$ = internal energy utilization weights
$\boldsymbol{\Lambda_s}$ = internal constraint weights
$\boldsymbol{\Lambda_{s,c}}$ = internal constraint weights (control)
$\boldsymbol{\Lambda_x}$ = internal reference state weights
$\boldsymbol{\Lambda_{x,c}}$ = internal reference states weights (control)
$\underline{\boldsymbol{\phi}}$ = controller design variables
$\overline{\boldsymbol{\phi}}$ = upper bound on controller design variables
$\underline{\boldsymbol{\phi}}$ = lower bound on controller design variables
$\boldsymbol{\phi^*}$ = optimally identified controller design variable values
$\boldsymbol{\phi'}$ = nominal controller design variable values
$\boldsymbol{\Phi}$ = edge design matrix for discrete plant design variables
$\boldsymbol{\Phi_c}$ = capacitance design matrix for discrete plant design variables
$\boldsymbol{\Psi}$ = edge design matrix for continuous plant design variables
$\boldsymbol{\Psi_c}$ = capacitance design matrix for continuous plant design variables

Subscripts

en = energy utilization
max = maximum
min = minimum
sc = state constraint violations
size = component sizing
st = state tracking
tot = total

References

[1] U.S. Energy Information Administration, 2020, "Annual Energy Outlook 2020 with Projections to 2050," U.S. Energy Information Administration, Office of Energy Analysis, U.S. Department of Energy, Washington, DC.
[2] Offer, G. J., 2015, "Automated Vehicles and Electrification of Transport," Energy Environ. Sci., **8**(1), pp. 26–30.
[3] Khaligh, A., and D'Antonio, M., 2019, "Global Trends in High-Power On-Board Chargers for Electric Vehicles," IEEE Trans. Veh. Technol., **68**(4), pp. 3306–3324.
[4] Ahmad, A., Alam, M. S., and Chabaan, R., 2018, "A Comprehensive Review of Wireless Charging Technologies for Electric Vehicles," IEEE Trans. Transp. Electrif., **4**(1), pp. 38–63.
[5] Wheeler, P., and Bozhko, S., 2014, "The More Electric Aircraft: Technology and Challenges," IEEE Electrif. Mag., **2**(4), pp. 6–12.
[6] Bennion, K., 2017, *Electric Motor Thermal Management Research, Annual Report*, National Renewable Energy Lab (NREL), Golden, CO.
[7] Rahn, C. D., and Wang, C.-Y., 2013, *Battery Systems Engineering*, Wiley, Hoboken, NJ.
[8] Rugh, J. P., Pesaran, A., and Smith, K., 2011, "Electric Vehicle Battery Thermal Issues and Thermal Management Techniques," SAE 2011 Alternative Refrigerant and System Efficiency Symposium, Scottsdale, AZ, Sept.
[9] Bailey, C., 2008, "Thermal Management Technologies for Electronic Packaging: Current Capabilities and Future Challenges for Modeling Tools," 10th Electronics Packaging Technology Conference, Singapore, Dec. 9–12, pp. 527–532.
[10] Allam, A., Onori, S., Marelli, S., and Taborelli, C., 2015, "Battery Health Management System for Automotive Applications: A Retroactivity-Based Aging Propagation Study," American Control Conference, Chicago, IL, July 1–3, pp. 703–715.
[11] Kirschbaum, F., Back, M., and Hart, M., 2002, "Determination of the Fuel-Optimal Trajectory for a Vehicle Along a Known Route," IFAC Proc., **35**(1), pp. 235–239.
[12] Moura, S. J., Fathy, H. K., Callaway, D. S., and Stein, J. L., 2011, "A Stochastic Optimal Control Approach for Power Management in Plug-In Hybrid Electric Vehicles," IEEE Trans. Control Syst. Technol., **19**(3), pp. 545–555.
[13] Leroy, T., Malaize, J., and Corde, G., 2012, "Towards Real-Time Optimal Energy Management of HEV Powertrains Using Stochastic Dynamic Programming," IEEE Vehicle Power and Propulsion Conference, Seoul, South Korea, Oct. 9-12, pp. 383–388.
[14] Serrao, L., Onori, S., and Rizzoni, G., 2009, "ECMS as a Realization of Pontryagin's Minimum Principle for HEV Control," American Control Conference, St. Louis, MO, June 10–12, pp. 3964–3969.
[15] Paganelli, G., Delprat, S., Guerra, T. M., Rimaux, J., and Santin, J. J., 2002, "Equivalent Consumption Minimization Strategy for Parallel Hybrid Powertrains," IEEE 55th Vehicular Technology Conference, Birmingham, AL, May 6-9, pp. 2076–2081.
[16] Jalil, N., Kheir, N. A., and Salman, M., 1997, "A Rule-Based Energy Management Strategy for a Series Hybrid Vehicle," American Control Conference, Albuquerque, NM, June 4-6, pp. 689–693.
[17] Banvait, H., Anwar, S., and Chen, Y., 2009, "A Rule-Based Energy Management Strategy for Plug- in Hybrid Electric Vehicle (PHEV)," American Control Conference, St. Louis, MO, June 10–12, pp. 3938–3943.
[18] Chekan, J. A., Bashash, S., and Taheri, S., 2018, "A Data-Driven Control Strategy for Trip Length-Conscious Power Management of Plug-In Hybrid Electric Vehicles," IEEE Conference on Control Technology and Applications (CCTA 2018), Copenhagen, Denmark, Aug. 21–24, pp. 794–799.
[19] Xie, S., Hu, X., Qi, S., and Lang, K., 2018, "An Artificial Neural Network-Enhanced Energy Management Strategy for Plug-In Hybrid Electric Vehicles," Energy, **163**, pp. 837–848.
[20] Yue, M., Jemei, S., Gouriveau, R., and Zerhouni, N., 2019, "Review on Health-Conscious Energy Management Strategies for Fuel Cell Hybrid Electric Vehicles: Degradation Models and Strategies," Int. J. Hydrogen Energy, **44**(13), pp. 6844–6861.
[21] Moura, S. J., Stein, J. L., and Fathy, H. K., 2013, "Battery-Health Conscious Power Management in Plug-in Hybrid Electric Vehicles Via Electrochemical Modeling and Stochastic Control," IEEE Trans. Control Syst. Technol., **21**(3), pp. 679–694.
[22] Romijn, T. C. J., Donkers, M. C. F., Kessels, J. T., and Weiland, S., 2018, "A Distributed Optimization Approach for Complete Vehicle Energy Management," IEEE Trans. Control Syst. Technol., **27**(3), pp. 964–980.
[23] Padovani, T. M., Debert, M., Colin, G., and Chamaillard, Y., 2013, "Optimal Energy Management Strategy Including Battery Health through Thermal Management for Hybrid Vehicles," IFAC Proc., **46**(21), pp. 384–389.
[24] Doshi, N., Hanover, D., Hemmati, S., Morgan, C., and Shahbakhti, M., 2019, "Modeling of Thermal Dynamics of a Connected Hybrid Electric Vehicle for Integrated HVAC and Powertrain Optimal Operation," ASME Paper No. DSCC2019-9223.
[25] Huang, Y., Wang, H., Khajepour, A., He, H., and Ji, J., 2017, "Model Predictive Control Power Management Strategies for HEVs: A Review," J. Power Sources, **341**, pp. 91–106.
[26] Vahidi, A., Stefanopoulou, A., and Peng, H., 2006, "Current Management in a Hybrid Fuel Cell Power System: A Model-Predictive Control Approach," IEEE Trans. Control Syst. Technol., **14**(6), pp. 1047–1057.
[27] Koeln, J. P., Pangborn, H. C., Williams, M. A., Kawamura, M. L., and Alleyne, A. G., 2019, "Hierarchical Control of Aircraft Electro-Thermal Systems," Trans. Control Syst. Technol., pp. 1218–1232.
[28] Docimo, D. J., Pangborn, H. C., and Alleyne, A. G., 2018, "Hierarchical Control for Electro-Thermal Power Management of an Electric Vehicle Powertrain," ASME Paper No. DSCC2018-9215.
[29] Dunham, W., Hencey, B., Girard, A. R., and Kolmanovsky, I., 2019, "Distributed Model Predictive Control for More Electric Aircraft Subsystems Operating at Multiple Time Scales," IEEE Trans. Control Syst. Technol., **28**, pp. 2177–2190.
[30] Amini, M. R., Kolmanovsky, I., and Sun, J., 2020, "Hierarchical MPC for Robust Eco-Cooling of Connected and Automated Vehicles and Its Application to Electric Vehicle Battery Thermal Management," IEEE Trans. Control Syst. Technol., **29**(1), pp. 316–328.
[31] Park, S., 2011, *A Comprehensive Thermal Management System Model for Hybrid Electric Vehicles*, University of Michigan, Ann Arbor, MI.
[32] Patil, R., Adornato, B., and Filipi, Z., 2010, "Design Optimization of a Series Plug-in Hybrid Electric Vehicle for Real-World Driving Conditions," SAE Int. J. Eng., **3**(1), pp. 655–665.
[33] Assanis, D., Delagrammatikas, G., Fellini, R., Filipi, Z., Liedtke, J., Michelena, N., Papalambros, P., Reyes, D., Rosenbaum, D., Sales, A., and Sasena, M., 1999, "Optimization Approach to Hybrid Electric Propulsion System Design," Mech. Struct. Mach., **27**(4), pp. 393–421.
[34] Bayrak, A. E., Ren, Y., and Papalambros, P. Y., 2016, "Topology Generation for Hybrid Electric Vehicle Architecture Design," ASME J. Mech. Des., **138**(8), p. 081401.
[35] Silvas, E., Hofman, T., Serebrenik, A., and Steinbuch, M., 2015, "Functional and Cost-Based Automatic Generator for Hybrid Vehicles Topologies," IEEE/ASME Trans. Mechatronics, **20**(4), pp. 1561–1572.
[36] Nagel, B., Böhnke, D., Gollnick, V., Schmollgruber, P., Rizzi, A., La Rocca, G., and Alonso, J. J., 2012, "Communication in Aircraft Design: Can We Establish a Common Language?," 28th International Congress of the Aeronautical Sciences, Brisbane, Australia, Sept. 23–28, pp. 1–13.
[37] McCullers, L. A., 1984, "Aircraft Configuration Optimization Including Optimized Flight Profiles," NASA Langley Research Center Recent Experiences in Multidisciplinary Analysis and Optimization, Part 1, pp. 395–412.
[38] Tappeta, R. V., Nagendra, S., and Renaud, J. E., 1999, "A Multidisciplinary Design Optimization Approach for High Temperature Aircraft Engine Components," Struct. Optim., **18**(2–3), pp. 134–145.
[39] Allison, J. T., and Herber, D. R., 2014, "Multidisciplinary Design Optimization of Dynamic Engineering Systems," AIAA J., **52**(4), pp. 691–710.
[40] Silvas, E., Hofman, T., Murgovski, N., Etman, L. F. P., and Steinbuch, M., 2017, "Review of Optimization Strategies for System-Level Design in Hybrid Electric Vehicles," IEEE Trans. Veh. Technol., **66**(1), pp. 57–70.

[41] Fathy, H. K., Reyer, J. A., Papalambros, P. Y., and Ulsoy, A. G., 2001, "On the Coupling Between the Plant and Controller Optimization Problems," Proc. Am. Control Conf., **3**, pp. 1864–1869.
[42] Wipke, K., Markel, T., and Nelson, D., 2001, "Optimizing Energy Management Strategy and Degree of Hybridization for a Hydrogen Fuel Cell SUV," Proceedings of 18th Electric Vehicle Symposium, Berlin, Germany.
[43] Murgovski, N., Johannesson, L., Sjöberg, J., and Egardt, B., 2012, "Component Sizing of a Plug-in Hybrid Electric Powertrain Via Convex Optimization," Mechatronics, **22**(1), pp. 106–120.
[44] Bayrak, A. E., Kang, N., and Papalambros, P. Y., 2016, "Decomposition-Based Design Optimization of Hybrid Electric Powertrain Architectures: Simultaneous Configuration and Sizing Design," ASME J. Mech. Des., **138**(7), p. 071405.
[45] Kim, M. J., and Peng, H., 2006, "Combined Control/Plant Optimization of Fuel Cell Hybrid Vehicles," Proc. Am. Control Conf., **2006**, pp. 496–501.
[46] Sanchez-Sanchez, K. B., and Ricardez-Sandoval, L. A., 2013, "Simultaneous Design and Control Under Uncertainty Using Model Predictive Control," Ind. Eng. Chem. Res., **52**(13), pp. 4815–4833.
[47] Brengel, D. D., and Seider, W. D., 1992, "Coordinated Design and Control Optimization of Nonlinear Processes," Comput. Chem. Eng., **16**(9), pp. 861–886.
[48] Rafieishishavan, S., 2020, *Integration of Design and Control for Large-Scale Applications: A Back-Off Approach*, University of Waterloo, Waterloo, ON, Canada.
[49] Koeln, J. P., Williams, M. A., Pangborn, H. C., and Alleyne, A. G., 2016, "Experimental Validation of Graph-Based Modeling for Thermal Fluid Power Flow Systems," ASME Paper No. DSCC2016-9782.
[50] Williams, M. A., Koeln, J. P., Pangborn, H. C., and Allenye, A. G., 2017, "Dynamical Graph Models of Aircraft Electrical, Thermal, and Turbomachinery Components," ASME J. Dyn. Syst. Meas. Control, **140**(4), p. 041013.
[51] Docimo, D. J., and Alleyne, A. G., 2018, "Electro-Thermal Graph-Based Modeling for Hierarchical Control With Application to an Electric Vehicle," IEEE Conference on Control Technology and Applications, Copenhagen, Denmark.
[52] Pangborn, H. C., and Alleyne, A. G., 2019, "Cooperativity and Hierarchical MPC of State-Constrained Switched Power Flow Systems," Proceedings of the American Control Conference, American Automatic Control Council, Philadelphia, PA, July 10–12, pp. 4245–4252.
[53] Docimo, D. J., Kang, Z., James, K. A., and Alleyne, A. G., 2020, "A Novel Framework for Simultaneous Topology and Sizing Optimization of Complex, Multi-Domain Systems-of-Systems," ASME J. Mech. Des., **142**(9), p. 091701.
[54] Messac, A., 2015, *Optimization in Practice With MATLAB for Engineering Students and Professionals*, Cambridge University Press, New York.
[55] Laird, C., Docimo, D. J., Aksland, C. T., and Alleyne, A. G., 2020, "Graph-Based Design and Control Optimization of a Hybrid Electrical Energy Storage System," ASME Paper No. DSCC2020-3233.
[56] Pangborn, H. C., Koeln, J. P., Williams, M. A., and Alleyne, A. G., 2018, "Experimental Validation of Graph-Based Hierarchical Control for Thermal Management," ASME J. Dyn. Syst. Meas. Control, **140**(10), p. 101016.
[57] Aksland, C., 2019, *Modular Modeling and Control of a Hybrid Unmanned Aerial*, University of Illinois at Urbana-Champaign, Urbana, IL.